COSMIC VARIANCE AND ITS EFFECT ON THE LUMINOSITY FUNCTION DETERMINATION IN DEEP HIGH-z SURVEYS

M. TRENTI

Space Telescope Science Institute, 3700 San Martin Drive Baltimore MD 21218; trenti@stsci.edu

AND

M. STIAVELLI

Space Telescope Science Institute, 3700 San Martin Drive, Baltimore, MD 21218; and Department of Physics and Astronomy,
Johns Hopkins University, Baltimore, MD 21218; mstiavel@stsci.edu

ABSTRACT

We study cosmic variance in deep high-redshift surveys and its influence on the determination of the luminosity function for high-redshift galaxies. For several survey geometries relevant for *Hubble Space Telescope* (*HST*) and *James Webb Space Telescope* (*JWST*) instruments, we characterize the distribution of the galaxy number counts. This is obtained by means of analytic estimates via the two-point correlation function in extended Press-Schechter theory, as well as by using synthetic catalogs extracted from *N*-body cosmological simulations of structure formation. We adopt a simple luminosity-dark halo mass relation to investigate the effects of environment on the fitting of the luminosity function. We show that in addition to variations of the normalization of the luminosity function, a steepening of its slope is also expected in underdense fields, similar to what is observed within voids in the local universe. Therefore, to avoid introducing artificial biases, caution must be taken when attempting to correct for field underdensity, such as in the case of the *HST* UDF *i*-dropout sample, which exhibits a deficit of bright counts with respect to the average counts in GOODS. A public version of the cosmic variance calculator based on the two-point correlation function integration is available on the Web at STScI.

Subject headings: galaxies: high-redshift — galaxies: statistics — large-scale structure of universe

Online material: color figures

1. INTRODUCTION

Deep high-redshift observations are providing a unique insight into the early stages of galaxy formation, when the universe was no more than one billion years old. Large samples of galaxies at $z > 5$ exist and allow us to study with unprecedented detail the early epoch of galaxy assembly and star formation history (see, e.g., Steidel et al. 1996; Madau et al. 1996; Giavalisco 2002; Bouwens et al. 2004; Mobasher et al. 2005; Beckwith et al. 2006; Oesch et al. 2007), as well as to constrain the properties of sources responsible for reionization (see, e.g., Stiavelli et al. 2004; Yan & Windhorst 2004; Bunker et al. 2006). Hunting for high-z galaxies usually follows two complementary approaches. One can either conduct large-area surveys, such as GOODS (Giavalisco et al. 2004) and, especially, COSMOS (Scoville et al. 2007), where the luminosity limit is about L_*, or focus on small areas of the sky, such as has been done for the Hubble Deep Field (HDF; Williams et al. 1996) and Ultra-Deep Field (UDF; Beckwith et al. 2006). In the latter case, the magnitude limit is 2.5–3 mag below L_* (UDF limit), and the aim is primarily to probe the faint end of the luminosity function. While this strategy has a good payoff in terms of galaxy detections, particularly when the slope of the luminosity function approaches 2 near the magnitude limit of the observations, the field of view of these pencil-beam surveys is usually rather small, with the edge of the order of a few hundred arcseconds. Therefore, the number counts are significantly influenced by cosmic variance (see, e.g., Somerville et al. 2004). For example, the surface density of *i*-dropouts at the GOODS depth found in one of the two HUDF-NICMOS parallel fields (GO 9803, PI: Thompson; identified as HUDFP2 in Bouwens et al. 2006) is only one-third of the average value from all the 30 ACS

fields in GOODS (Bouwens et al. 2006). Even considering the much larger area of one GOODS field (about $10' \times 16'$), the expected 1 σ uncertainty in the number counts for Lyman break galaxies at $z \approx 6$ is still $\approx 20\%$ (Somerville et al. 2004).

Relatively little effort has so far been devoted to quantifying the impact of cosmic variance on the determination of properties of high-redshift galaxies. Past studies have generally characterized only the variance of the number counts of a given cosmic volume (Mo & White 1996; Colombi et al. 2000; Newman & Davis 2002; Somerville et al. 2004) or studied the full distribution, but only in numerical simulations appropriate for local galaxies (Szapudi et al. 2000). The impact of cosmic variance on the measurement of the shape of the luminosity function at high redshift has never been addressed, despite the fact that it is known that there is an environmental dependence in the local universe, as M_* in voids is about 1 magnitude fainter than in the field (Hoyle et al. 2005). Our goal is to highlight the problem and to provide methods for addressing it.

In this paper we estimate the variance of the number counts using extended Press-Schechter analysis, and we compute the distribution of number counts in synthetic surveys generated by using a Monte Carlo pencil-beam tracer in snapshots from cosmological *N*-body simulations. Our runs follow the evolution of dark matter particles only. Galaxy luminosities are linked to the dark matter mass by adopting the parametric models by Vale & Ostriker (2004) and Cooray & Milosavljević (2005), which provide quite realistic output luminosity function. This numerical approach allows us to investigate how the best-fitting parameters of the luminosity function depend on the environment probed.

The paper is organized as follows. In § 2 we define cosmic variance and compute it using the extended Press-Schechter

formalism. In § 3 we describe the numerical framework that we adopt to investigate cosmic variance. In § 4 we apply the Monte Carlo code to characterize the number counts for a variety of high-z surveys strategies, while in § 5 we investigate the impact of number counts variance on the determination of the luminosity function, focusing in particular on the faint-end slope of i-dropout galaxies in the UDF main and parallel fields. We give our conclusions in § 6.

2. LARGE-SCALE STRUCTURE AND UNCERTAINTIES IN GALAXY NUMBER COUNTS

The number counts of galaxies in a survey are affected by a combination of discrete sampling, observational incompleteness, and large-scale structure. Given a probability distribution $p(N)$ for the number counts with mean $\langle N \rangle$ and variance $\langle N^2 \rangle$, we define the total fractional error of the counts N as

$$v_r = \frac{\sqrt{\langle N^2 \rangle - \langle N \rangle^2}}{\langle N \rangle}. \tag{1}$$

The uncertainties in excess to Poisson shot noise are usually quantified in terms of a relative "cosmic variance" (e.g., see Newman & Davis 2002; Somerville et al. 2004), defined as

$$\sigma_v^2 \equiv \frac{\langle N^2 \rangle - \langle N \rangle^2}{\langle N \rangle^2} - \frac{1}{\langle N \rangle}. \tag{2}$$

To evaluate the relative cosmic variance σ_v^2 of a given sample, two main theoretical approaches are possible: (1) estimation based on the two-point correlation function $\xi(r)$ of the sample, or (2) direct measurement using mock catalogs from cosmological simulations of structure formation.

In the first case, σ_v^2 is derived from $\xi(r)$ as follows (e.g., see Peebles 1993):

$$\sigma_v^2 = \frac{\int_V \int_V d^3x_1 \, d^3x_2 \, \xi(|\boldsymbol{x}_1 - \boldsymbol{x}_2|)}{\int_V \int_V d^3x_1 \, d^3x_2}, \tag{3}$$

where the integration is carried out over the volume V observed by the survey. The two-point correlation function $\xi(r)$ can be derived from either a cosmological model for the growth of density perturbations (e.g., see Newman & Davis 2002), or a simpler analytical model, such as a power law, with free parameters fixed by observational data (e.g., see Somerville et al. 2004). This method has the advantage of requiring small computational resources, limited to the evaluation of the multidimensional integral in equation (3), while being able to handle an arbitrarily large survey volume of any geometry. The main limitation is that only the second moment of the counts probability distribution $p(N)$ can be obtained. This method also relies on an input two-point correlation function that is typically evaluated only considering linear evolution of density perturbations (see, however, Peacock & Dodds [1996] for an analytical model of the non-linear evolution of the power spectrum). In addition, this framework assumes that all the survey volume is at a given redshift, which may not be appropriate for high-redshift ($z > 5$) Lyman break galaxy observations, where the pencil beam extends for about $\Delta z \approx 1$, an interval over which there is evidence of evolution of the galaxy luminosity function (see, e.g., Bouwens et al. 2006).

A direct measurement of $p(N)$ from N-body simulations bypasses all these limitations, but requires significant computational resources. In particular, the cosmic volume simulated must be much larger than the survey volume, which in practice sets a limit on the survey area that can be adequately modeled.

To summarize, if one is interested primarily in computing a total error budget on the number counts of a survey, the estimate of σ_v^2 through integration of $\xi(r)$ may be sufficient and requires relatively little effort. However, in this paper we combine both methods, emphasizing especially the construction of mock catalogs from N-body simulations, as this is required to address the influence of cosmic variance on the uncertainty in the shape of the luminosity function.

2.1. Cosmic Variance in Extended Press-Schechter Theory

Following Newman & Davis (2002), we estimate the cosmic variance in linear theory evaluating the integral of equation (2) using $\xi(r)$ derived from the transfer function of Eisenstein & Hu (1999). For a given redshift z, the halo–dark matter bias $b(M_h)$ as a function of the halo mass (M_h) is evaluated using the Sheth & Tormen (1999) formalism. The total average bias of the sample is then computed by averaging $b(M_h)$ over the Sheth & Tormen (1999) mass function down to a mass limit set by matching the desired comoving number density of halos.

These are the basic steps to evaluate the influence of cosmic variance in the error budget of the number counts using linear theory.

1. *Define the survey volume and its average redshift z_{av}*. For example, for Lyman break galaxy dropouts samples, this is set by the combination of the field-of-view angular size and the redshift window for the dropout selection.

2. *Choose the intrinsic number of objects in the survey.* This can be done, for example, either starting from a specific luminosity function or by estimating the number of expected objects from the actual number of observed objects divided by their completeness ratio.

3. *Estimate the average incompleteness*. Incompleteness will be close to 0 for selections much brighter than the magnitude limit of the survey, but can be in the range 0.3–0.5 when pushing detections up to the limit of the data (Oesch et al. 2007). A precise estimate generally requires object-recovery Monte Carlo simulations.

4. *Adopt a value for the average target-halo filling factor*. This is in general smaller than 1, as a specific class of objects may be visible only for a limited period of time. For example, in the case of Lyman break galaxies, the duty cycle may be as low as 0.25 (see, e.g., Verma et al. 2007).

The input information above is then used to estimate the total fractional uncertainty on the number counts as follows.

1. *Compute the minimum halo mass M_{min} required to obtain the number density of halos hosting the survey population*. Combining the halo filling factor and the intrinsic number of objects in the survey (given the survey volume), we compute the minimum halo mass in the Sheth & Tormen (1999) model required to match the input number density.

2. *Compute the average bias of the sample*. We calculate the average bias of the sample using the Press-Schechter model (Press & Schechter 1974).

3. *Integrate the dark matter $\xi(r)$ over the survey volume*. The dark matter two-point correlation function is integrated over the pencil-beam geometry of the volume (cf. eq. [3]; see also Newman & Davis 2002) to obtain the dark matter cosmic variance σ_{DM}^2.

4. *Multiply σ_{DM} by the average galaxy bias* to obtain the cosmic variance of the sample: $\sigma_v^2 = b^2 \sigma_{DM}^2$.

5. *Take into account Poisson noise for the number of observed objects*. The total error budget is given by combining the contribution from cosmic variance, which is an intrinsic property of the

underlying galaxy population, with the observational uncertainty related to the actual number of observed objects, N_{obs}. Therefore, the total fractional error (that is, the 1 σ uncertainty) is

$$v_r = \sqrt{\sigma_v^2 + 1/N_{obs}}. \quad (4)$$

In § 4 we use this method to estimate the number counts uncertainty for typical high-redshift surveys.

3. SYNTHETIC SURVEYS

In this section we present the numerical framework based on cosmological simulations that we developed to address the influence of cosmic variance on high redshift observations.

3.1. *N-Body Simulations*

The numerical simulations have been carried out using the public version of the PM-tree code Gadget-2 (Springel 2005). We adopt a cosmology based on the third year *WMAP* data (Spergel et al. 2007): $\Omega_\Lambda = 0.74$, $\Omega_m = 0.26$, $H_0 = 70$ km s^{-1} Mpc^{-1}, and $\sigma_8 = 0.75$ (or $\sigma_8 = 0.9$; see below), where Ω_m is the total matter density in units of the critical density [$\rho_c = 3H_0^2/(8\pi G)$], H_0 is the Hubble constant (parameterized as $H_0 = 100$ h km s^{-1} Mpc^{-1}), G is Newton's gravitational constant (Peebles 1993), Ω_Λ is the dark energy density, and σ_8 is the rms mass fluctuation in a sphere of radius 8 Mpc h^{-1} extrapolated to $z = 0$ using linear theory. The initial conditions have been generated with a code based on the Grafic algorithm (Bertschinger 2001) using a ΛCDM transfer function computed via the fit by Eisenstein & Hu (1999) with spectral index $n_s = 1$.

A summary of our *N*-body runs is presented in Table 1. We resort to various box sizes, optimized for different survey geometries. To characterize small-area surveys such as a single ACS field, we use a box of edge 100 Mpc h^{-1} simulated with 512^3 particles. This choice gives us a volume about 73 times larger than the effective volume probed by one ACS field for *V*-dropouts [$\approx 5.7 \times 5.7 \times 420$ (Mpc $h^{-1})^3$] and about 86 times larger for *i*-dropouts ($\approx 6 \times 6 \times 320$ (Mpc $h^{-1})^3$]. The single particle mass is 5×10^8 $M_\odot$ h^{-1} and guarantees that the host halos that we consider ($M_{halo} \gtrsim 2 \times 10^{10}$ $M_\odot$ h^{-1}) are resolved with at least 40 particles in the deepest survey that we simulate. To investigate the cosmic variance in larger area, less deep surveys, such as GOODS, we use instead a larger box, of size 160 Mpc h^{-1}, also simulated with 512^3 particles. The total volume of the simulation is about 26 times larger than a single *i*-dropout GOODS field [$\approx 17.6 \times 28.1 \times 320$ (Mpc $h^{-1})^3$]. The single-particle mass for this run is 2×10^9 $M_\odot$ h^{-1}. These simulations have $\sigma_8 = 0.75$. In addition, we consider a higher resolution simulation with more than twice the number of particles of our basic runs ($N = 680^3 \approx 3.1 \times 10^8$), and with a box of edge 128 Mpc h^{-1} that starts with $\sigma_8 = 0.9$. This simulation has a single-particle mass of 4.4×10^8 $M_\odot$ h^{-1}.

Dark matter halos are identified in the simulations snapshots (saved every $\Delta z = 0.125$ in the redshift interval 10−4.5) using the HOP halo finder (Eisenstein & Hut 1998), with the following parameters: the local density around each particle is constructed using a 16 particle smoothing kernel, while for the regrouping algorithm we use $\delta_{peak} = 200$, $\delta_{saddle} = 170$, $\delta_{outer} = 100$, and a minimum group size of 40 particles. The halo mass distribution in the snapshots is well described (with displacements within $\approx 25\%$) by a Sheth & Tormen (1999) mass function. One limitation that has to be taken into account when estimating the cosmic variance from *N*-body simulations is the cosmic variance of the complete simulation volume. For example, in our 512^3 particle,

N	L_{box} (Mpc h^{-1})	σ_8
512^3	100	0.75
512^3	160	0.75
680^3	128	0.9

Note.—Summary of the *N*-body simulations of structure formation. The first column reports the number of particles *N* used, the second the box the edge size (L_{box}), and the third the normalization σ_8 of the amplitude of the power spectrum of density fluctuations.

100 Mpc h^{-1} edge box run there are 2620 dark matter halos at $z = 6$ with more than 100 particles, and the differences in this number from run to run are larger than the nominal Poisson variance. We checked this effect by carrying out a control run with the same initial conditions but a different seed for the random number generator, obtaining a difference of $\approx 6\%$. The use of a larger box and 680^3 particles in our highest resolution run is expected to reduce run-to-run variations, but we cautiously assume a 10% relative uncertainty in the value of the cosmic variance that we derive through this paper.

In addition, in the 680^3 simulation we also save snapshots at intervals $\Delta z = 0.5$ from $z = 10$ to $z = 15$ in order to provide a preliminary characterization of cosmic variance in future *JWST* NIRCam surveys.

3.2. *Pencil-Beam Tracing*

Our pencil-beam tracer is similar to the one developed by Kitzbichler & White (2007), but it is optimized for high *z* surveys, allowing us in particular to take advantage of the quasi-constant angular distance versus redshift relation. We trace through the simulation box a parallelepiped where the base is a parallelogram, whose size is given by the field of view of the survey in comoving units, and the depth is the comoving depth associated with the redshift uncertainty of the selection window for Lyman break galaxies we are interested in. This choice means that we are neglecting the variation of angular distance versus redshift in the redshift interval of the selection window considered. For example, the comoving edge of the ACS field of view for *V*-dropouts is 5.5 Mpc h^{-1} at $z = 4.6$ and 5.9 Mpc h^{-1} at $z = 5.7$, and we approximate it with 5.7 Mpc h^{-1}. The pencil beam is traced through different snapshots as we swipe through its depth, and, consistent with our angular size approximation, we assume an average value for Δz (the redshift difference between two snapshots) expressed in comoving distance. The choice to save snapshots at $\Delta z = 0.125$ implies that a single beam passes through several different snapshots, so that the evolution in the halo mass function is well captured. The interval $\Delta z = 0.125$ is equivalent to about 40 Mpc h^{-1} at $z = 6$, and the evolution in the number density of halos at the same mass scale between two adjacent snapshots is of the order 10%–15%. The beam starts at a random position within the simulation volume and then proceeds through the cube with periodic boundary conditions, angled using the following choices for the two direction angles θ_1 and θ_2:

$$\tan \theta_1 = 0.3, \qquad \tan \theta_2 = 0.5.$$

These values have been selected to guarantee no superposition and adequate spacing for a typical *HST*/ACS Lyman break dropout beam as it wraps around the simulation box due to the periodic initial conditions. The linear correlation between the number

TABLE 2
PENCIL BEAM PROPERTIES

ID	Angular Size (arcsec^2)	z_{min}	z_{max}	Comoving Size (Mpc h^{-1})^3	Separation
ACS v-dropout	205×205	4.6	5.7	$5.7 \times 5.7 \times 420$	...
ACS i-dropout	205×205	5.65	6.7	$6.0 \times 6.0 \times 320$	...
GOODS i-dropout	600×960	5.65	6.7	$17.6 \times 28.1 \times 320$	...
NIC3 z-dropout	51×51	7.0	8.5	$1.6 \times 1.6 \times 342$	...
WFC3 z-dropout	125×137	7.0	8.5	$3.9 \times 4.3 \times 342$	...
NIC3 J-dropout	51×51	8.5	10.0	$1.7 \times 1.7 \times 269$	...
WFC3 J-dropout	125×137	8.5	10.0	$4.1 \times 4.5 \times 269$	...
JW F115W-dropout	$2 \times (130 \times 130)$	9.0	10.8	$2 \times (4.5 \times 4.5 \times 295)$	$30'' \equiv 1.0$ Mpc h^{-1}
JW F150W-dropout	$2 \times (130 \times 130)$	11.0	12.7	$2 \times (4.6 \times 4.6 \times 217)$	$30'' \equiv 1.0$ Mpc h^{-1}
JW F200W-dropout	$2 \times (130 \times 130)$	12.9	15.1	$2 \times (4.8 \times 4.8 \times 223)$	$30'' \equiv 1.1$ Mpc h^{-1}

NOTE.—Assumed properties for the pencil beam fields used throughout this paper.

counts of two nearby segments of the beam, estimated using the two-point correlation function (see § 2.1), is in fact ≲0.02.

Finally, all the dark matter halos within the beam are flagged and saved for subsequent processing by the halo occupation distribution part of the Monte Carlo code. A complete description of the properties of the pencil-beam surveys simulated in this paper is given in Table 2.

3.3. Halo Occupation Distribution

Dark matter halos within a simulated field of view are populated with galaxies according to a simple halo occupation distribution (HOD) model. We assume an average occupation number (Wechsler et al. 2001)

$$\langle N_{gal} \rangle = \theta(M - M_{min})\left[1 + (M/M_1)^{\beta}\right], \quad (5)$$

where $\theta(x)$ is the Heaviside step function, M_{min} is a minimum halo mass threshold, M_1 is the typical scale where multiple galaxies are present within the same halo, and $\beta > 0$ is of order unity. If $M > M_{min}$, one galaxy is placed at the center of the halo, and then the number of companions is extracted from a Poisson distribution with mean $(M/M_1)^{\beta}$. Of these galaxies a fraction f_{ON} are finally identified as Lyman break galaxies (this is to take into account possible observational incompleteness and/or a duty cycle where LBGs are on only for a fraction of their lifetime).

We show in Figure 1 the distribution of the number counts for i-dropouts in one ACS field at the UDF depth. We consider: (1) $f_{ON} = 1$, $M_1 \to +\infty$ (that is, one galaxy per halo); (2) $f_{ON} = 0.5$ and $f_{ON} = 0.25$, $M_1 \to +\infty$ (that is, one galaxy per halo with either 0.25 or 0.5 detection probability); and (3) $f_{ON} = 1$, $M_1 = 5 \times 10^{11} M_\odot h^{-1}$ and $\beta = 1$. In addition, we also investigate the effect of changing the box size, the resolution, and the σ_8 value of the N-body simulations using both our $N = 512^3$ and our $N = 680^3$ runs. The value of M_{min} is kept as free parameter, and it is adjusted to have the same average number of counts in all three cases. The required variations of M_{min} are limited within a factor of 2. The distribution of the number counts probability is very similar in the four cases (see Table 3 for v_r values) and shows that the characterization of the cosmic variance versus the average number counts is solid with respect to the details of the modeling. This is essentially due to the fact that by changing M_{min} by a factor of 2, the average bias of the sample varies by only less than 15%. This is reassuring, as there are large theoretical uncertainties on modeling high-redshift galaxy formation.

3.4. Field of View Geometry

The importance of correctly modeling the geometry of the field of view to quantify the cosmic variance is shown by Figure 2. Here we focus on a single snapshot at $z = 6.125$, and we measure the total fractional error v_r of number counts in a volume of 11520 (Mpc h^{-1})^3 with different shapes. From Figure 2, v_r is largest in the quasi-cubical volume and smallest for the pencil beam. Therefore, cosmic variance computed only from the total volume of the survey, assumed to be a sphere as in Somerville et al. (2004), is overestimated. This is because a narrow and long pencil beam probes many different environments, while a cubic volume may sit for a significant fraction of its volume on either underdense or overdense regions. In all cases shown in Figure 1, the total error exceeds Poisson noise, and the contribution from cosmic variance is dominant, especially when the average number of counts in the volume is much larger than 1. Figure 2 also shows an excellent agreement between the measurement from
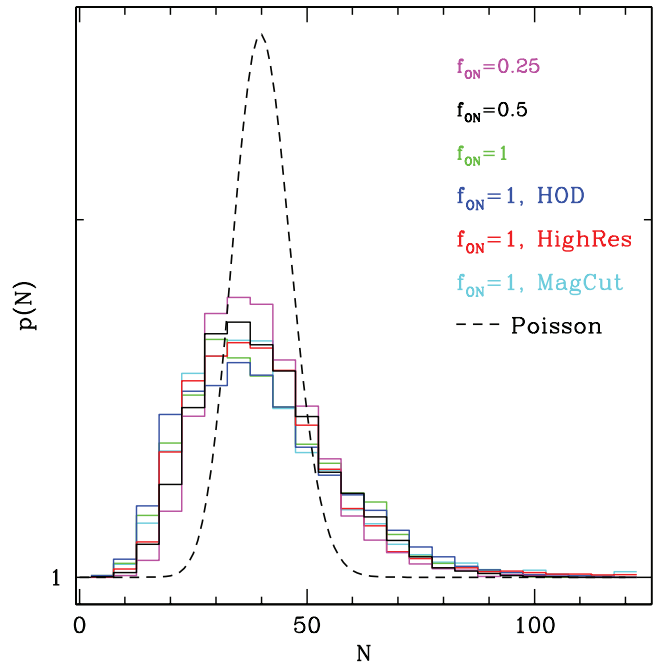

FIG. 1.—Probability distribution of the i-dropouts number counts for an ACS field with 40.3 average counts, using different halo occupation models and different simulations boxes: $N = 512^3$ and $N = 680^3$ (HighRes). The cosmic variance for these runs is quantified in Table 3. For reference, the Poisson distribution for 40.3 counts on average is plotted with a dashed line.

TABLE 3
Cosmic Variance for the Models in Figure 1

ID	v_r
f_{ON} = 0.25, HighRes	0.32
f_{ON} = 0.5	0.35
f_{ON} = 1	0.39
f_{ON} = 1, HOD	0.42
f_{ON} = 1, HighRes	0.40
f_{ON} = 1, HighRes, MagCut	0.42

Note.—Cosmic variance v_r for i-dropouts (40 counts on average) in one ACS field for the different models presented in Fig. 1.

cosmological simulations and the analytical estimate using the two-point correlation function.

3.5. *Luminosity-Mass Relation*

Our numerical simulations follow the evolution of dark matter only; therefore, we have to assume a mass-luminosity relation to investigate the influence of the cosmic variance on the determination of the luminosity function. For this we extend to higher redshift the fitting formulas used by Vale & Ostriker (2004) and Cooray & Milosavljević (2005), adopting

$$L(M) = L_0 \frac{(M/M_s)^a}{[q + (M/M_s)^{cd}]^{1/d}}, \quad (6)$$

and assuming $M_s = 10^{11} M_\odot$, $a = 4.0$, $q = 0.57$, $c = 3.57$, and $d = 0.23$; L_0 is conventionally set to 1. As the main goal of this paper is not to provide a detailed modeling of the mass-luminosity relation, but rather to investigate the dependence of the luminosity function parameters on the environment and on the fitting method adopted, the simple modeling of equation (6) appears adequate.

For a fully consistent representation of the observational selection process for Lyman break galaxies, it would be necessary to apply a luminosity cut in the apparent and not in the absolute magnitude. The apparent luminosity-distance relation does in fact evolve quite significantly over a redshift range $\Delta z \approx 1$ (see, e.g., Bouwens et al. 2006, their Fig. 7). This effect leads to a reduction of the effective volume of the survey and thus to an increase of the cosmic variance contribution to the count's uncertainty. This is because dropouts tend to be preferentially selected in the low-redshift corner of the selection window, even if luminosity evolution with redshift will partially offset this trend, as galaxies at higher z appear to have a higher L/M ratio (see Cooray 2005). In our standard model for number count uncertainty from numerical simulations, we apply a cutoff in mass (that is, in absolute magnitude), which gives us a framework consistent with the estimates from the two-point correlation function. To evaluate the error introduced by this assumption, we have implemented a cutoff in observed magnitude for an ACS i-dropout sample with 40 detections on average constructed from our cosmological simulation at high resolution and using the relation between observed L_* and redshift z as plotted in Figure 7 of Bouwens et al. (2006). The resulting number count distribution is plotted in Figure 1. The total fractional uncertainty in the number counts is only marginally higher (0.42 vs. 0.40) than in the case where a cutoff in absolute magnitude is applied.

4. COSMIC VARIANCE

4.1. *HST Surveys*

The results from our simulated distribution of number counts for different high-redshift surveys are reported in Figures 3, 4,
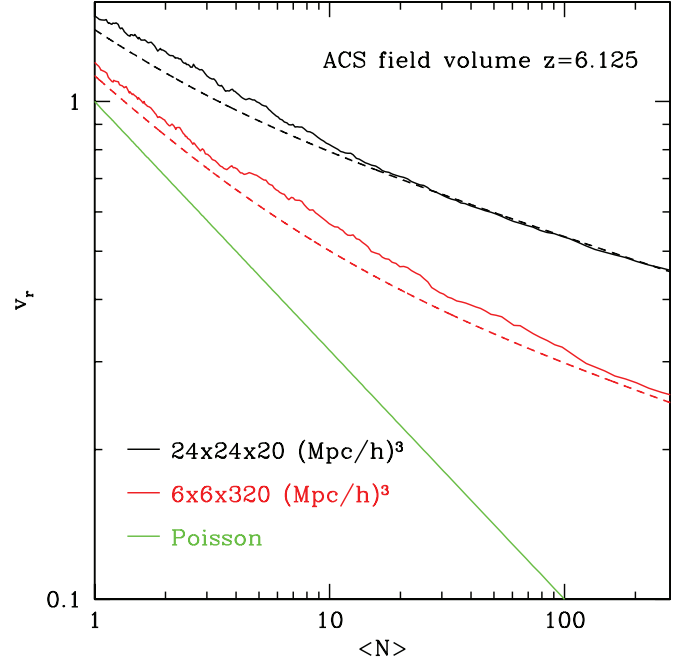

Fig. 2.— Total fractional error v_r of the number counts of dark matter halos in a cosmic volume of 1.152×10^4 (Mpc $h^{-1})^3$ at $z = 6.125$ as a function of the average number counts for different shapes of the volume. The solid line is the measurement from our numerical simulations, and the dashed line is the prediction using the analytic model described in § 2.1. The quasi-cubic volume has the highest standard deviation, especially at large number counts, where the Poisson noise (*green line*) has a negligible contribution to the total fractional error (see also Fig. 4).

and 5. For a given survey geometry, we plot the fractional number counts uncertainty v_r as a function of their average value. This facilitates the application to surveys at different depths. Given that the details of the halo occupation model have only a modest influence on the value of v_r (see Fig. 1), we resort in this paper to a reference model of one galaxy per halo, with $f_{ON} = 1$ (i.e., unit probability of detection) unless otherwise noted. In addition, we highlight the expected total fractional uncertainty on the number counts due to Poisson noise only.

At the typical number counts for a field at the UDF depth, the total fractional uncertainty is $v_r \approx 25\%$ for V-dropouts (assuming 100 detections per field; see Oesch et al. 2007) and $v_r \approx 35\%$ for i-dropouts (assuming 50 detections per field; see Beckwith et al. 2006). This is much smaller than the Poisson noise associated with the average realized number counts. Therefore, cosmic variance is the dominant source of uncertainty for UDF-like deep fields. At lower number counts per field of view, that is, when the survey is shallower, the Poisson contribution to the total fractional uncertainty v_r increases (see Fig. 4), until it becomes dominant at the limit of zero average counts. The agreement between v_r estimated using the two-point correlation function and that measured in the numerical simulations is very good. The framework is also consistent with the observed clustering of high-redshift galaxies, such as measured by Overzier et al. (2006): our standard recipe for populating dark matter halos with galaxies gives an average galaxy–dark matter bias $b = 5.0$ for an ACS i-dropout sample with 60 detections on average, a value within the one sigma error bar in the measurement by Overzier et al. (2006). Note however that the large observational uncertainties do not allow a more detailed quantitative comparison.

From the full probability distribution on the number counts, derived from our simulations, we can also evaluate the likelihood of finding a factor 2 overdensity in galaxies at $z = 5.9 \pm 0.2$ in the UDF field, as reported by Malhotra et al. (2005). If
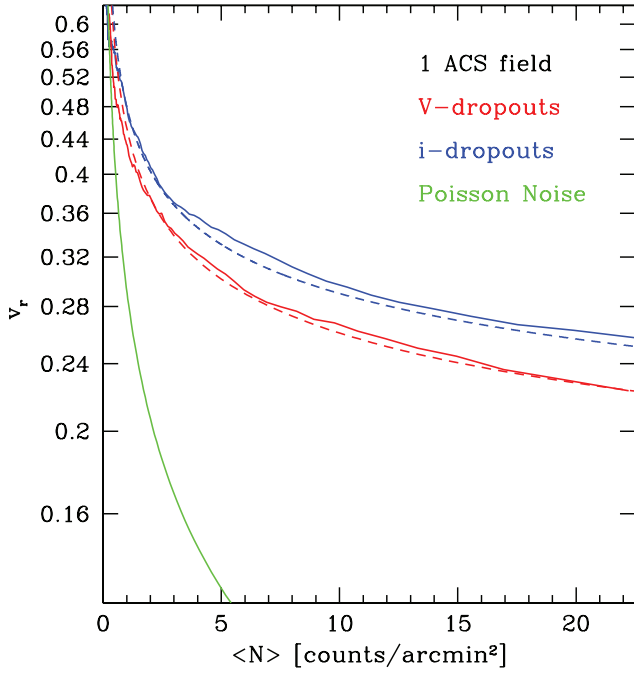
FIG. 3.—Total fractional uncertainty v_r of the number counts estimated using model (*dotted lines*) and simulations (*solid lines*) for V (*red*) and i (*blue*) dropouts for one ACS field (in units of the average number of counts) vs. the average number of counts per arcmin². The Poisson noise associated to the counts is plotted for reference in green.

we assume that the expected number of galaxies in that redshift interval is 7.5, the fractional uncertainty in the counts turns out to be $v_r \approx 67\%$, and the probability of 15 or more realized counts in that redshift interval is greater than 10% (this has been measured taking advantage of the full probability distribution obtained
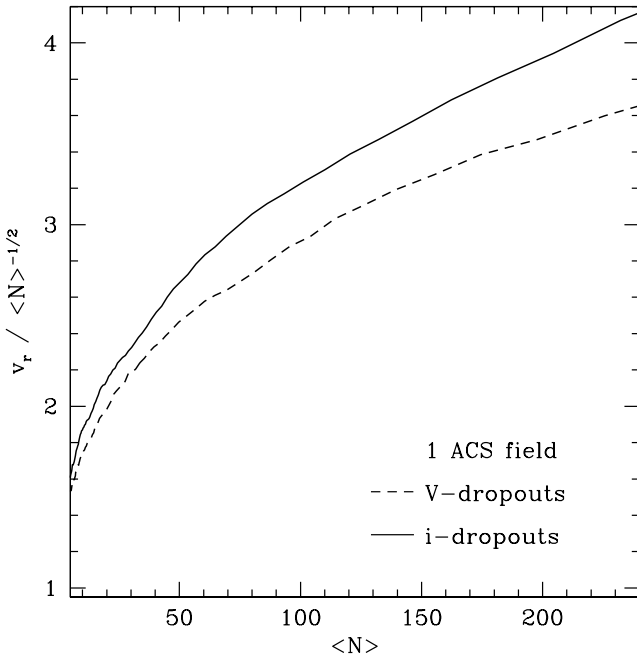

FIG. 4.—Total fractional error (v_r) in the number counts for V and i-dropouts in one ACS field in units of the Poisson noise ($\langle N \rangle^{-1/2}$) vs. the average number of counts ($\langle N \rangle$) per field. As v_r is much bigger than the corresponding Poisson noise, cosmic variance is the dominant source of uncertainty in the number counts. [*See the electronic edition of the Journal for a color version of this figure.*]
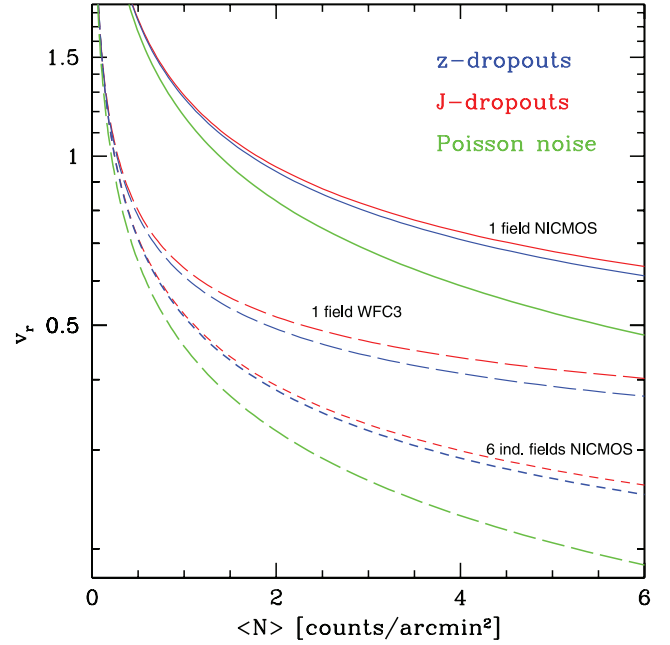

FIG. 5.—As in Fig. 4 (all curves from analytical modeling), but for z and J-dropouts considering different fields of view: NICMOS Camera 3 (*solid lines*), six independent NICMOS Camera 3 fields summed (*short-dashed lines*), and one WFC3 field (*long-dashed lines*). Poisson noise for a single NICMOS Camera 3 and WFC3 field is shown in green.

through the simulations). Therefore, the measured fluctuation, while lying outside the standard deviation, is not exceptional. Given that an i-dropout selection window contains about five intervals of width $\Delta z = 0.2$, one overdensity such as that observed by Malhotra et al. (2005) will be present in a significant number of random pointings.

To characterize the number count uncertainty in the larger area GOODS survey, we resort to the simulation with edge 160 Mpc h^{-1}, whose results are reported in Figure 6 for the combination of the two North and South fields. Here v_r is consistent with the estimate using the two-point correlation function within a relative difference of 10% at most. Interestingly, the i-dropout cosmic variance in one GOODS field is not too different from that for a smaller but deeper UDF field. This is due to two effects: (1) the increased sensitivity of the UDF enables to detect fainter Lyman break galaxies and thus to probe the distribution of smaller mass halos that are progressively less clustered, and (2) there is a significant correlation between the counts in adjacent fields.

To better quantify this latter effect, we plot in Figure 7 the linear correlation coefficient between the i-dropouts counts in two nearby ACS fields:

$$r_{\mathrm{lin}} = \frac{\sigma_{12}}{\sqrt{\sigma_{11}\sigma_{22}}}, \qquad (7)$$

where

$$\sigma_{ab} = \langle (ab - \langle ab \rangle)^2 \rangle. \qquad (8)$$

The linear correlation has been computed using the analytical model from the two-point correlation function.

Two adjacent i-dropout fields at the UDF depth (50 counts on average) have a linear correlation in number counts of about 0.4. The correlation decreases rapidly as the separation increases, and fields separated by more than 500″ have $r_{\mathrm{lin}} < 0.05$. Therefore,
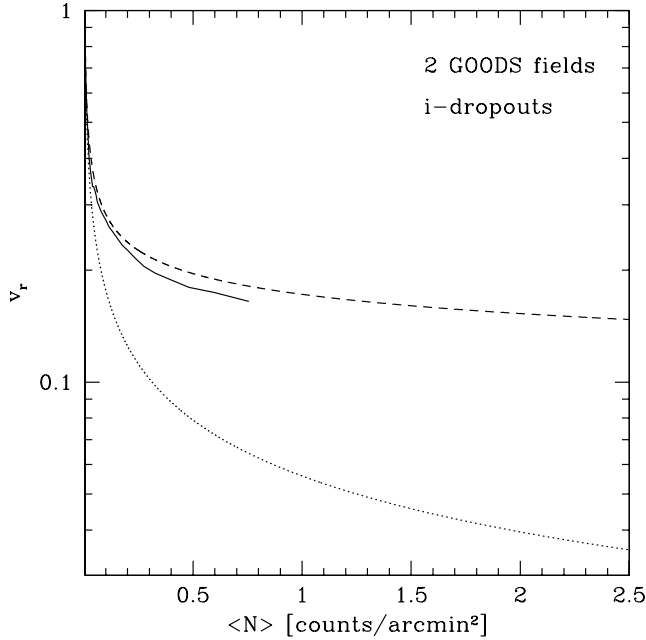
Fig. 6.—Total fractional error for *i*-dropouts in the two GOODS fields (*solid line*: simulations; *dashed line*: model) vs. the average number of counts per arcmin^2. Poisson noise is plotted for reference in green. [*See the electronic edition of the Journal for a color version of this figure.*]

Fig. 8.—Total fractional error v_r for *JWST* NIRCam dropouts (*filled symbols*) and average number of detections $\langle N \rangle$ per field of view (*open symbols*) vs. the average redshift of the passband filter. The total field of view is given by two 2.2×2.2 arcmin^2 fields separated by $30''$. The counts go down to a mass limit equivalent to a depth of 3 mag below M_* for *i*-dropouts in a ACS field assuming the Bouwens et al. (2006) luminosity function. For F200W and F150W dropouts v_r is dominated by Poisson noise, while for F115W v_r is about twice the Poisson error associated to the estimated 10 counts per field. [*See the electronic edition of the Journal for a color version of this figure.*]

HST parallel fields, typically separated by $550''$, are essentially independent from each other. With independent fields the variance of the total counts is given by the sum of the variances in each field (as the set of counts in the fields are independent variables).

For higher redshift Lyman break galaxies, we plot in Figure 5 the number count uncertainty within both NICMOS and WFC3 fields. A single NICMOS field has such a small area (≈ 0.72 arcmin^2) that v_r is dominated by Poisson noise up to a few counts per arcmin^2. The effect of cosmic variance in the
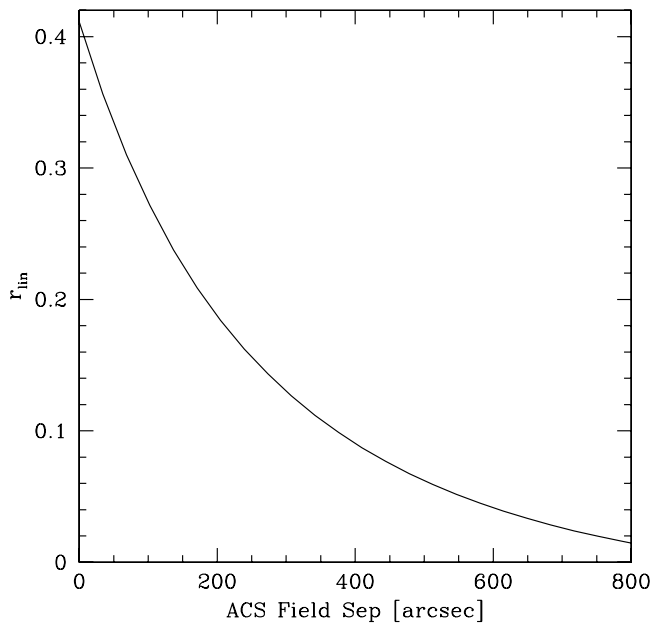

Fig. 7.—Linear correlation coefficient r_{lin} for the number counts of *i*-dropouts in two nearby ACS fields with an average of 50 detections per field, as function of their separation.
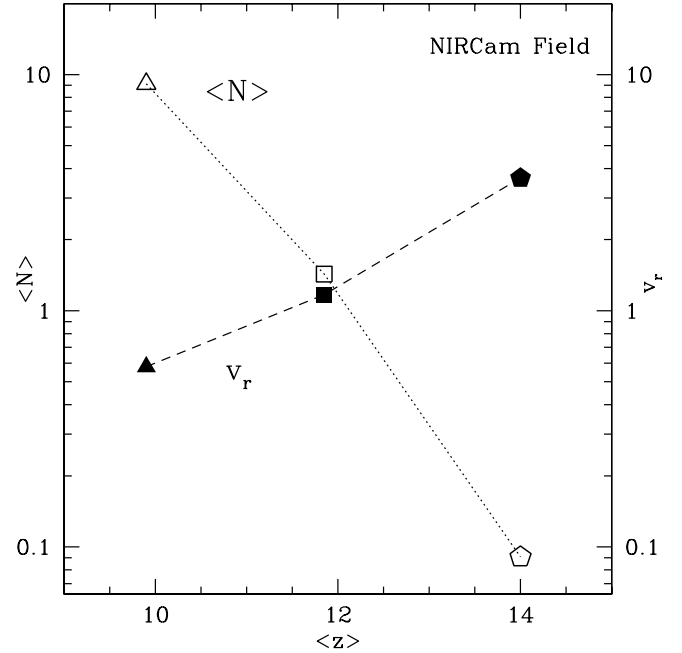
number counts uncertainty is instead more evident in a *HST*/WFC3–like field of view, where the uncertainty is significantly higher than Poisson noise. A very interesting conclusion that can be drawn from the figure is that the number counts uncertainty in the six independent main and parallel NICMOS fields, obtained through the HDF, HDF-South, UDF, and the UDF follow-up programs, is lower than that of one deep WFC3 field, despite covering slightly less area. This example nicely shows that in order to minimize cosmic variance effects in future surveys aimed at detecting $z > 7$ Lyman break galaxies, a sparse coverage is optimal. Of course, a continuous coverage has the advantage of enabling other science, such as weak-lensing studies at lower redshift.

4.2. *JWST Surveys*

As a preliminary characterization of cosmic variance in future *JWST* Lyman break galaxy surveys, we present in Figure 8 the cosmic variance for NIRCam F115W, F150W, and F200W dropouts as given by the combination of the two nearby fields of view of NIRCam (Gardner et al. 2006). This has been obtained assuming no evolution from the $z = 6 M/L$ relation (eq. [6]). The light cone has been traced through snapshots in our 680^3 particle run, considering dark matter halos down to 50 particles (that is, to a mass limit of $2.2 \times 10^{10}\, M_\odot\, h^{-1}$). If the same cutoff is applied to an ACS *i*-dropout survey, then we get about 250 *i*-dropouts per field of view (corresponding to a magnitude limit $m_{\mathrm{AB}} = 29.1$ using the Bouwens et al. 2006 luminosity function). As can be seen from Figure 8, the rapid evolution of the dark matter halo mass function greatly reduces the number of halos above the cutoff mass within the pencil beam at $z \gtrsim 10$. Therefore, the expected number of F200W dropout detections per NIRCam field is only $N \approx 0.1$, and these observations would be affected primarily by
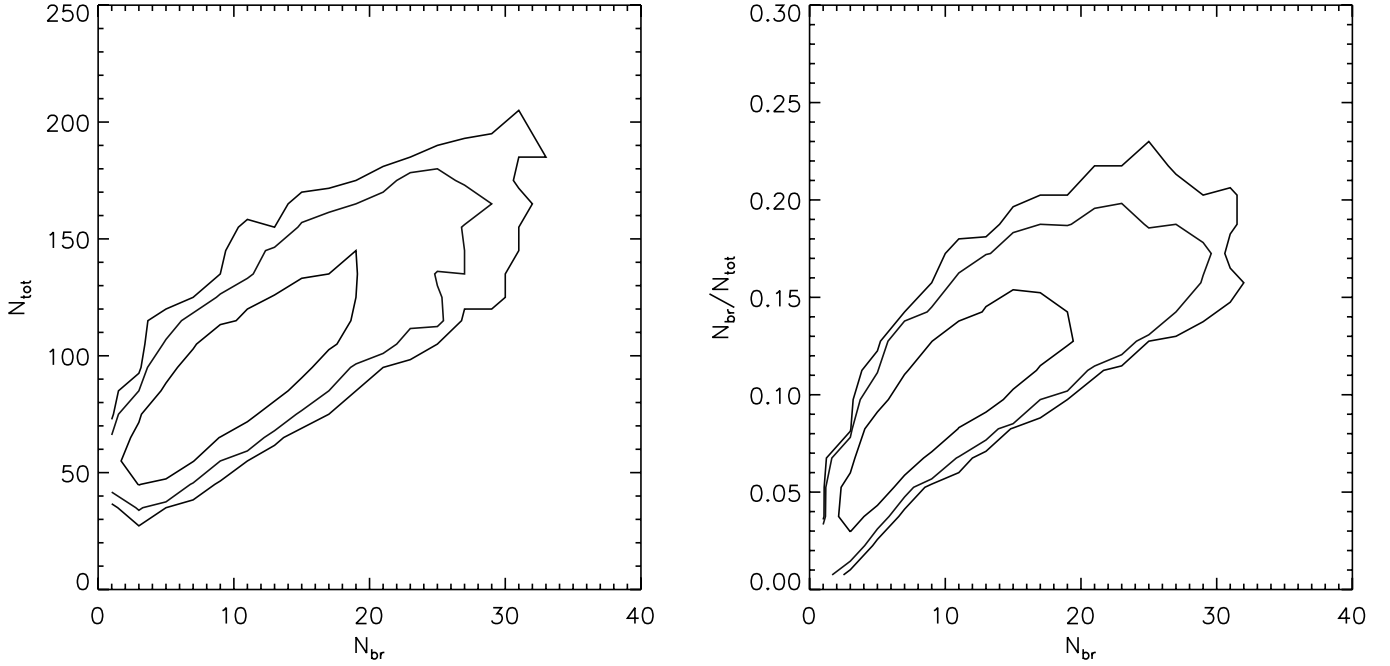
FIG. 9.—Distribution of the of the total (N_{tot}) vs. bright (N_{br}) i-dropouts counts (*left*) and of the N_{br}/N_{tot} ratio (*right*) simulated for one ACS field as a function of the number of bright counts. The plots have been obtained using 4000 MC realizations. Confidence level contours are 68% (*red*), 95% (*blue*), and 99% (*green*). The average number of bright counts per field is 1.0 arcmin^{-2}, while the average number of total counts is 8.6 arcmin^2. From the right panel it is clear that the steepness of the luminosity function increases in underdense regions. [*See the electronic edition of the Journal for a color version of this figure.*]

Poisson uncertainty. These numbers have been derived assuming a mass-luminosity relation of dropouts at $z > 6$ consistent with that of i-dropouts, as deep surveys with *JWST* are expected to reach about the $z = 6$ UDF sensitivity up to $z = 20$. Of course, it is quite possible that actual detections of F200W dropouts will be higher if these primordial galaxies are more luminous than their $z \approx 6$ counterparts, similar to what happens between $z = 0$ and $z = 6$ (e.g., see Cooray 2005). In addition, for a precise estimate of the expected number of these very high redshift objects in deep *JWST* surveys, a detailed modeling of the relation between intrinsic and observed luminosity is required. At least, however, dust reddening should play only a minor effect (see Trenti & Stiavelli 2006).

4.3. *Ground-based Narrowband Surveys*

If we consider narrowband searches for high-redshift galaxies, we typically have a different beam geometry, given by a large field of view with a small redshift depth. For example, Ouchi et al. (2005) detect more than 500 Lyα emitters at $z = 5.7 \pm 0.05$ in a 1 deg^2 area. Under these conditions, we estimate $v_r \approx 0.18$, more than 3 times the Poisson uncertainty of the counts. The large variance is given by a combination of a contiguous field of view with a small redshift interval, which gives a cosmic volume probed by this search roughly equivalent to that of a single 10×16 arcmin^2 i-dropout GOODS field.

5. INFLUENCE OF COSMIC SCATTER ON LUMINOSITY FUNCTION PARAMETERS

5.1. *Bright-Faint Counts and Environment*

The main influence of the environment probed by a deep field is on the observed number density of galaxies, and therefore on the normalization of the luminosity function. However, the shape of the luminosity function can also be affected. This is the case in the local universe, where it has been observed that the luminosity function in voids is steeper than in the field (see, e.g., Hoyle et al.

2005), but this possibility seems to be neglected when deriving the luminosity function for Lyman break galaxies (e.g., in Bouwens et al. 2006).

To highlight the importance of this effect even at high redshift, we plot in Figure 9 the distribution of massive halo ($M_{halo} > 1.2 \times 10^{11}$ $M_\odot$) counts versus total counts down to a lower mass halo limit ($M_{halo} > 3 \times 10^{10}$ $M_\odot$) for a simulated i-dropout survey with an ACS area. The average number of total counts is roughly at the Bouwens et al. (2006) UDF depth (8.6 counts per arcmin^2), while the counts for the more massive halos have an average density of ≈ 1 arcmin^{-2}, which is approximately the i-dropout number density in GOODS. The ratio of the massive to total counts can be adopted as an estimate for the steepness (i.e., the shape) of the luminosity function. From the right panel of Figure 9 it is clear that when the beam passes through underdense regions, the ratio easily decreases on average by more than a factor of 2, although a large scatter is present. This shows that the shape of the mass (luminosity) function does indeed depend on the environment.

To better understand the origin of this effect, we consider two idealized scenarios to model the relation between bright and total counts, where we consider only Poisson uncertainties. The first (see Fig. 10) has been obtained by assuming that the bright counts are completely uncorrelated with fainter ones. Therefore, we have

$$\langle N_{tot} \rangle = \langle N_{ft} \rangle + \langle N_{br} \rangle, \tag{9}$$

where $\langle N_{ft} \rangle$ (that is, the average difference between the total and bright counts) depends on the minimum mass cutoff mass considered. When $\langle N_{ft} \rangle \gg \langle N_{br} \rangle$, bright and total counts are almost uncorrelated, and therefore when a field is underdense in bright counts, total counts are almost unaffected, and its luminosity function appears on average (much) steeper. The luminosity function is instead (quasi-)shape-invariant when we consider
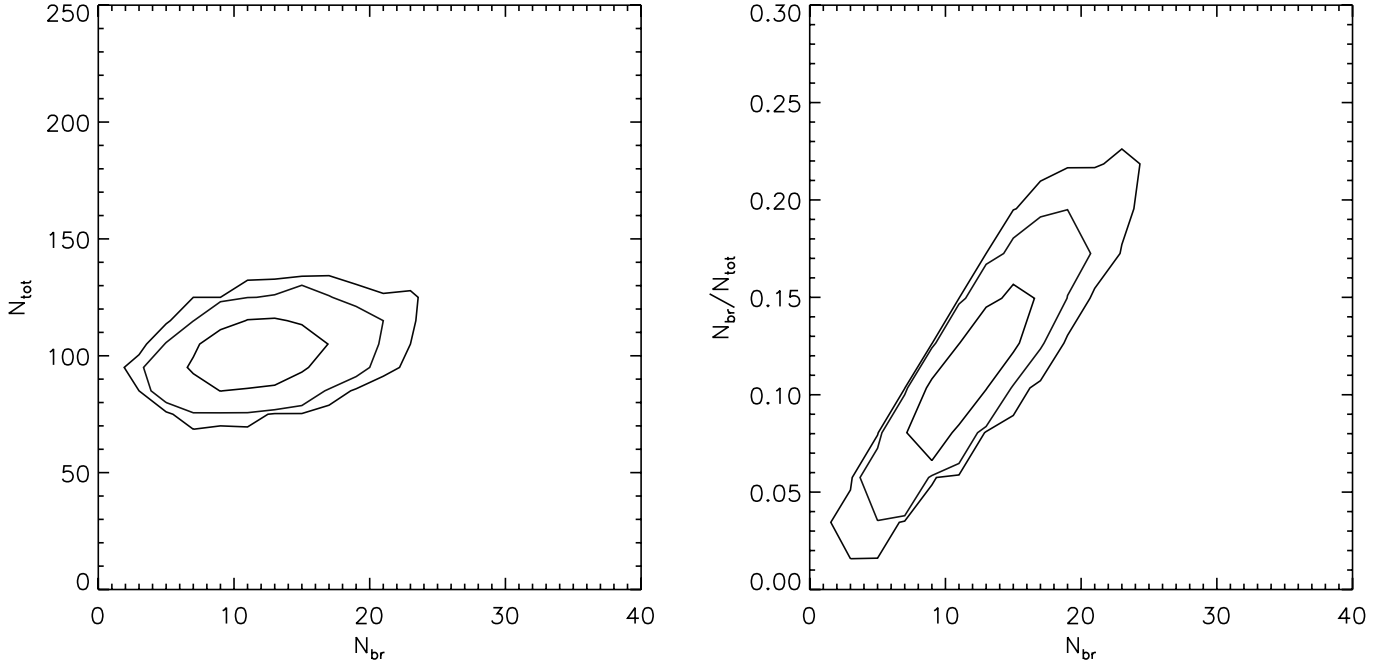
FIG. 10.—As in Fig. 9, but for a toy model where N_{ft} and N_{br} are uncorrelated. Here also, the luminosity function is steeper in underdense regions. [*See the electronic edition of the Journal for a color version of this figure.*]

a model with a total correlation between bright and total counts, where

$$\langle N_{tot} \rangle = \eta \langle N_{br} \rangle, \tag{10}$$

with η depending again on the minimum mass cutoff mass considered. The results for this model are shown in Figure 11 and have been obtained by first sampling the bright counts ($N_{br,i}$) from a Poisson distribution with average $\langle N_{br} \rangle$, and then sampling the faint counts $N_{ft,i}$ from a Poisson distribution with average

$pN_{br,i}$ and $p = 7.75$. This gives an average total number counts $\langle N_{tot} \rangle = 8.75 \langle N_{br} \rangle$.

A realistic distribution of the counts, such as that obtained from our mock catalogs, is shown in Figure 9 and lies between the two extreme cases considered as toy models. In particular, the low N_{br} behavior of the N_{br}/N_{tot} ratio is dominated by the correlation with N_{br}, as can be seen by comparing Figure 9 with Figure 10. This is because the large-scale structure introduces a correlation between bright and faint counts, but this correlation is not total. In fact, deeper surveys probe smaller mass halos, whose
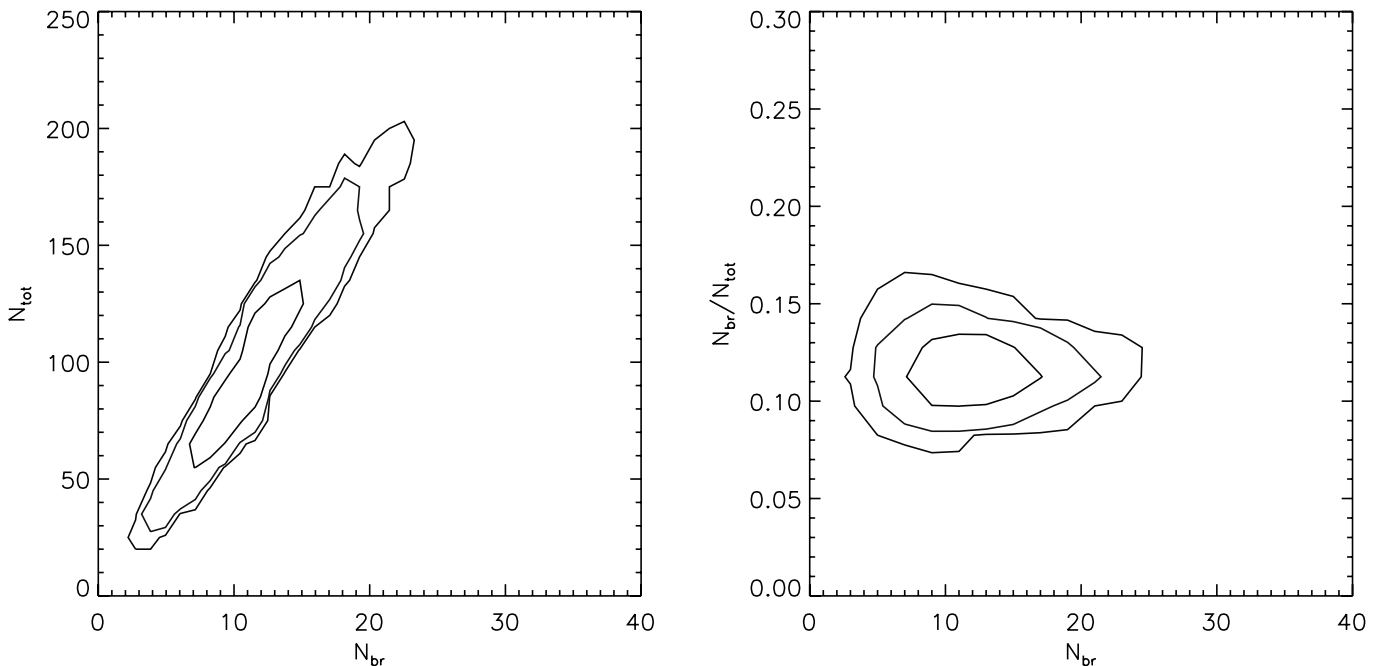

FIG. 11.—As in Fig. 9, but for a toy model where N_{ft} and N_{br} are perfectly linearly correlated, apart from Poisson fluctuations in N_{ft}. This correlation leads to a luminosity function shape that is environment-independent. [*See the electronic edition of the Journal for a color version of this figure.*]

formation probability is sensitive to higher frequencies in the power spectrum of primordial density perturbations than that for more massive halos targeted in shallower observations of the same field.

5.2. Luminosity Function Shape and Environment

The results of the previous section suggest that a more thorough characterization of the large-scale structure influence on the mass function at high redshift is required. Our main aim is to look for systematic variations depending on the realized number counts value and on the details of the fitting procedure employed. We fit a Schechter function in the form

$$\phi(L)dL = \phi_*(L/L_*)^{\alpha} \exp([-L/L_*])dL \qquad (11)$$

to the distribution of galaxy luminosity derived from the dark matter halo masses measured in our Monte Carlo code and transformed in luminosities using the prescription of equation (6). As discussed in § 3.5, our treatment to build a sample of galaxy luminosities is idealized, and we are missing many observational effects, such as apparent luminosity vs. redshift evolution and redshift-dependent selection effects within the redshift interval considered. Our main aim is to highlight the importance of large-scale structure in fitting the luminosity function, and not to construct a detailed representation of observations.

We start by considering, for a simulated V-dropout deep sample in one ACS field (200 galaxies on average in the pencil beam), the distribution of the Schechter function parameter L_* and α for 4000 Monte Carlo realizations.[1] We estimate the parameters using a standard maximum likelihood estimator on the unbinned detections, following essentially the procedure described in Sandage et al. (1979). For each synthetic catalog $\{L_i\}_{i=1,N}$ we compute the likelihood for the luminosity function in equation (11):

$$L(L_*, \alpha) = \prod_{i=1,N} \phi(L_i), \qquad (12)$$

where the ϕ_* is fixed by integrating the luminosity function up to the detection limit L_{min} of the survey and imposing the normalization

$$\int_{L_{min}}^{+\infty} \phi(L)\, dL = 1. \qquad (13)$$

The maximization of the likelihood $L(L_*, \alpha)$ is then carried out on a two-dimensional grid with spacing $\Delta\alpha = 0.01$ and $\Delta M_* = 0.025$, where $M_* = -2.5 \log L_*$. The resulting distribution of best-fitting parameters for the 4000 synthetic catalogs that we have generated are reported in Figure 12 and highlight the degeneration between the M_* and α parameters. By plotting L_* and α as a function of the number counts of the survey (Fig. 13), we can see that the slope of the luminosity function does not depend on the environment, while L_* does. When the number of counts in a field is above average, L_* is larger, although the scatter at any fixed number of counts is significant.

To further quantify the effect of cosmic scatter on the luminosity function fitting, we consider the case where Lyman break galaxies are detected both in a large-area deep survey, such as GOODS, and in a single, or a few, pencil beams at a greater depth, such as the UDF and UDF follow-up fields. This combination of data appears ideal from the observational point of view, as it allows us to constraint the break L_* of the luminosity function using detections from the large-area, shallower, survey, and the faint-end slope using the deeper data set. However, the fitting procedure employed may lead to artificial biases, especially if one tries to correct for the effects of cosmic variance by considering its effect on ϕ_* alone. In fact, one might be tempted to renormalize the luminosity function for the deeper fields by considering the number of dropout galaxies detected at the same depth of the larger area, fainter survey. For example, this is what has been done by Bouwens et al. (2006; see also Bouwens et al. 2007), who obtained the luminosity function for i-dropouts by multiplying the UDF and UDF parallel fields counts by factors of 1.3 and 1.5 (respectively) in order to account for a deficit of bright detections with respect to the GOODS fields. This correction has two potential problems that may contribute to introducing an artificial steepening of the luminosity function, and both problems are apparent from Figure 9. First, it is clear from the left panel of Figure 9 that if one were to rescale the luminosity function of the deeper field, a relation of the form $N_{ft} = \eta N_{br}$ would not be justified, as we show in § 5.1. In fact, the best-fitting linear relation for the counts in Figure 9 is $N_{ft} = 4.92 N_{br} + 47$. This implies that a 50% deficit in bright counts with respect to the average would correspond on average to only a 20% deficit in faint counts, and not to the 50% naive estimate of the deficit. There is also a second, subtler effect introduced by a renormalization of the luminosity function based on the number counts: N_{br}/N_{ft} is strongly correlated with N_{br} in underdense fields due to the lack of luminous galaxies, so a renormalization of the data based on matching the N_{br} counts to a reference value introduces an artificial steepening of the faint end of the luminosity function.

As a quantitative example, we consider a test case where the luminosity function is determined by GOODS-like data (one 10×16 arcmin² field) at the bright end and by one ACS field at the faint end. The average number counts per arcmin² that we
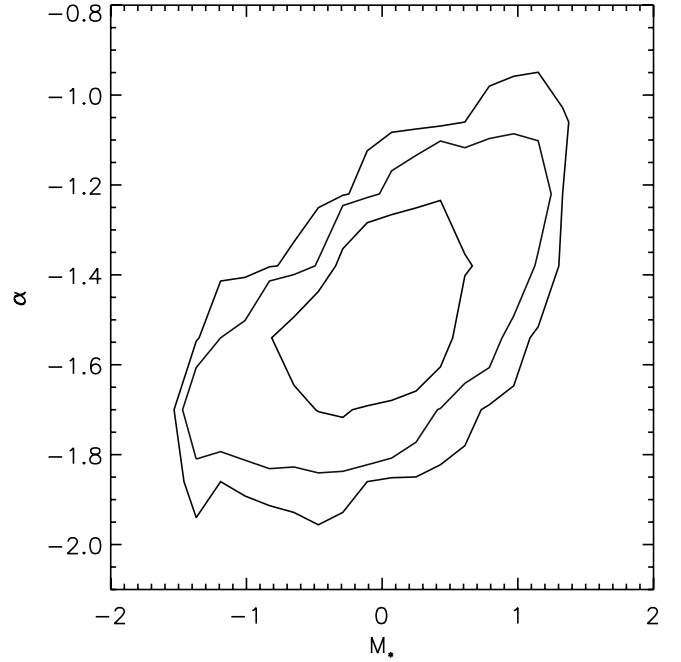

Fig. 12.— Best-fitting Schechter function parameters for V-dropouts from one ACS field with 200 average detections, simulated with 4000 realizations using our MC code. Parameters have been estimated using a maximum likelihood analysis. Confidence level contours are 68% (*red*), 95% (*blue*), and 99% (*green*). [*See the electronic edition of the Journal for a color version of this figure.*]

---

[1] We recall here that not all the 4000 realizations are truly independent, as the total volume of the box is only about 73 times larger than the pencil-beam volume for V-dropouts.
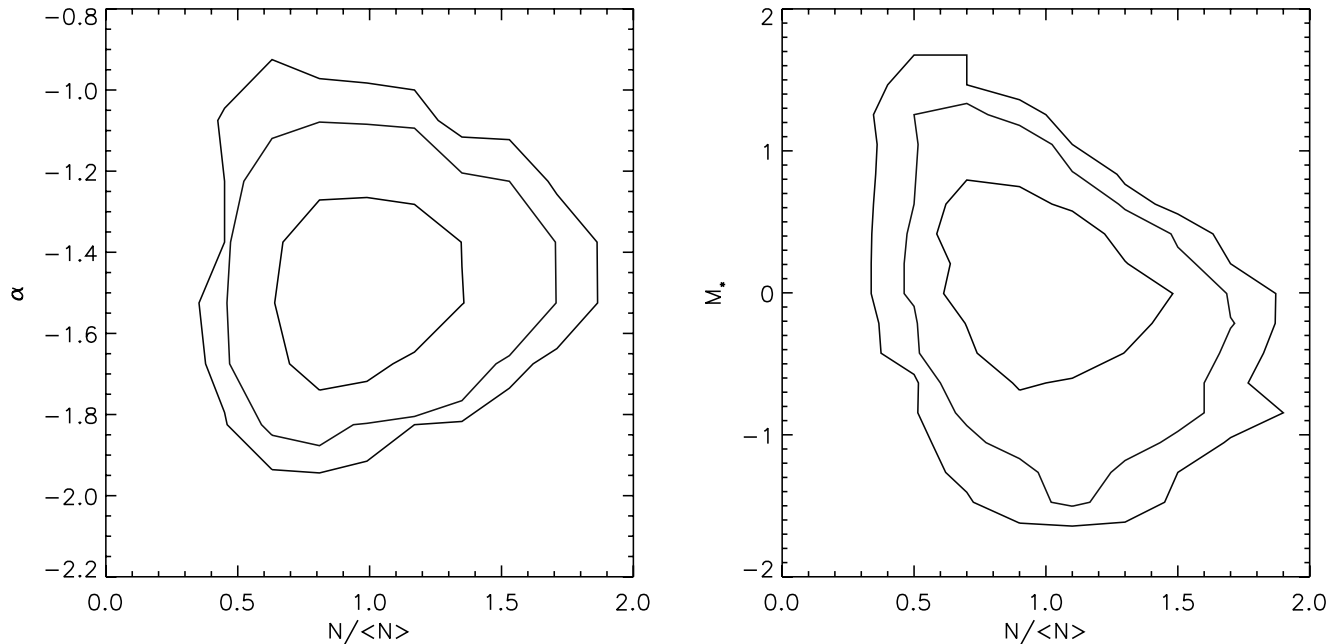
FIG. 13.—Maximum likelihood best-fitting Schechter function parameters as function of the number counts in the field of view for *V*-dropouts from one ACS field with an average of 200 detections, simulated with 4000 MC realizations. *Left*: α; *right*: M_*. Confidence level contours are 68% (*red*), 95% (*blue*), and 99% (*green*). [*See the electronic edition of the Journal for a color version of this figure.*]

adopt are 0.75 for the bright end and 8.75 for the deeper field (to be consistent with the number densities in Bouwens et al. 2006). This gives us an average of 120 bright objects in the large area field and of 100 objects down to the fainter limit of the UDF-like field.

The luminosity function is then fitted by adopting three different methods:

1. First, an observed luminosity function is constructed from the synthetic catalogs using binned data (0.5 mag bins) by combining the data from the two surveys with no large-scale structure correction, as described in § 5.3 of Bouwens et al. (2006). Then we fit the model luminosity function using a maximum likelihood approach to these binned data, that is, we compute the theoretical expectation for the number of objects in each magnitude bin and then maximize the likelihood under the assumption that the counts in each bin are Poisson distributed.

2. The maximum likelihood on binned data is found, as in point (1) above, but the luminosity function determination includes a large-scale correction (relying on the relation $N_{\rm ft} = \eta N_{\rm br}$), as in § 5.1 of Bouwens et al. (2006).

3. Unbinned maximum likelihood modeling of the data is done, with free normalization of the data between the deep and wide fields. The procedure is a straightforward generalization of the methods discussed above for determining the luminosity function in a single field, and proceeds as described in Sandage et al. (1979), where this method was first applied to luminosity function fitting.[2]

---

[2] Here we would like to stress that the Sandage et al. (1979) procedure relies on unbinned data, so the STY79 fitting adopted by Bouwens et al. (2007) is not really an application of this method. Note also that eq. (A6) in Bouwens et al. (2007) for the probability distribution of the counts in each bin is not the Poisson one, and the maximization of their likelihood returns a result equivalent to maximizing a Poisson probability distribution only in the limit of a perfect data-model match, that is, when the number of observed objects in each bin is equal to the number of expected objects. This difference is likely to affect the confidence regions for the best-fitting parameters.

The results from these different fitting methods are shown in Figure 14, where we plot the contour levels of the distribution of the best-fitting luminosity function parameters obtained from 600 different combinations of deep and wide fields. All the parameters are shown as a function of the total number counts in the deep field. The maximum likelihood method with free normalization between the two fields (Sandage et al. 1979) has a 1 σ uncertainty of ≈ 0.15 on α and of ≈ 0.3 on M_*. The uncertainties are similar when the fit is performed on binned data without using the large-scale renormalization of Bouwens et al. (2006), but in this case the fixed normalization between the two fields introduces a bias in α, with underdense deep fields leading to a shallower slope. Applying the environment renormalization following Bouwens et al. (2006) does overcorrect the problem with a larger uncertainty in α and M_* (0.21 and 0.36, respectively) and a preference for steeper shapes of the luminosity function. This is an artifact, as the faint end of the luminosity function is overestimated by the correction applied when the deep field is lacking luminous galaxies. This behavior is also apparent from the fits performed in Bouwens et al. (2007), e.g., in their Table 6 they estimate for *i*-dropouts $\alpha = -1.77 \pm 0.16$ using a maximum likelihood approach similar to Sandage et al. (1979) and $\alpha - 2.06 \pm 0.20$ using the large-scale renormalization method.

6. CONCLUSIONS

In this paper, we present detailed estimates of the variance in the number counts of Lyman break galaxies for high-redshift deep surveys and the resulting impact on the determination of the galaxy luminosity function. The number count distribution has been derived from collisionless, dark matter only cosmological simulations of structure formation assuming a M/L relation and has been compared with analytical estimates obtained from the two-point correlation function of dark matter halos. Halos have been identified in the simulation snapshots, saved at high frequency ($\Delta z = 0.125$ up to $z = 10$), and a pencil-beam tracer Monte Carlo code has been used to construct synthetic catalogs
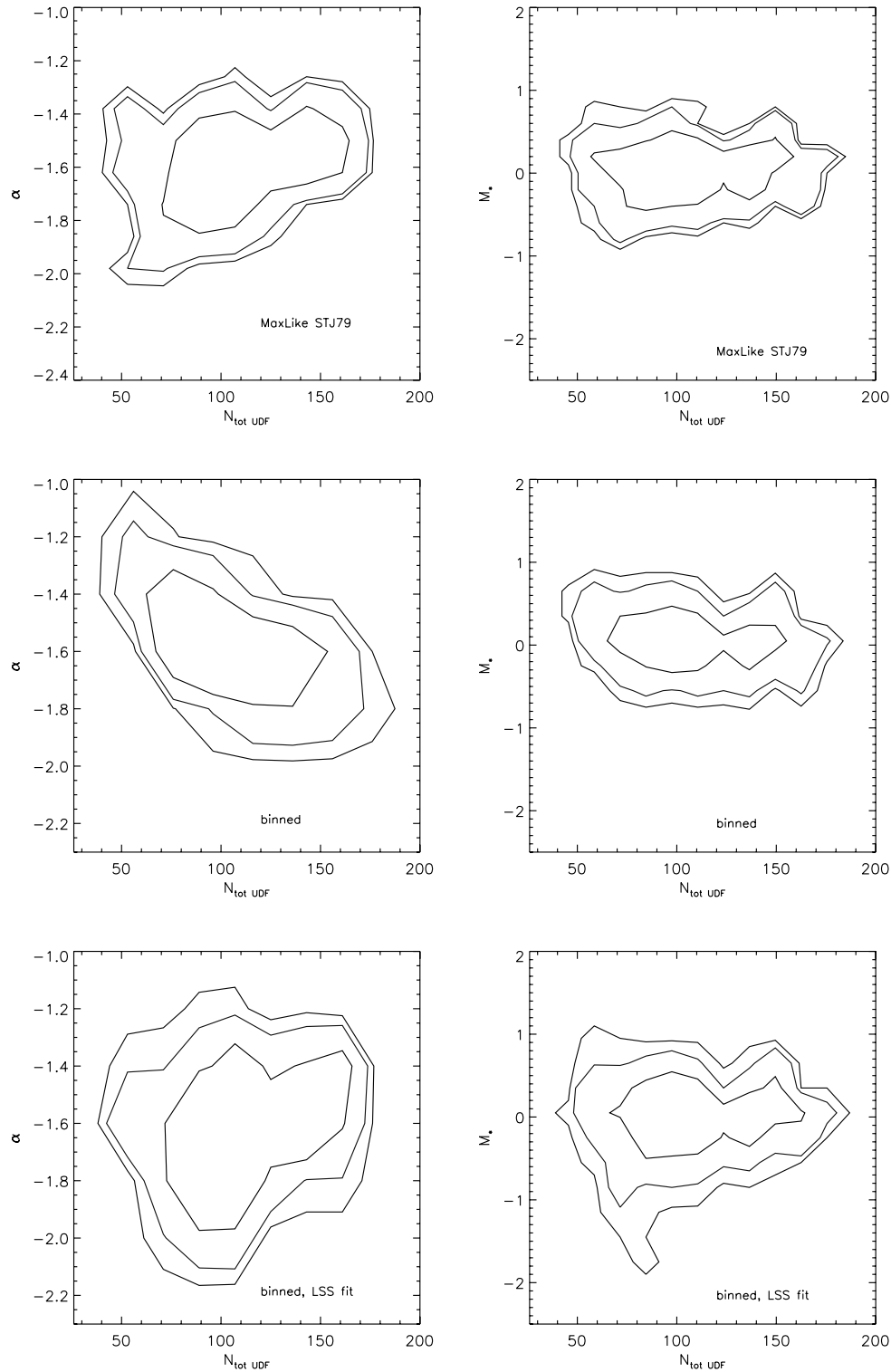
FIG. 14.—Best-fitting parameters α (*left*) and M_* (*right*) from unbinned *i*-dropout data (600 synthetic catalogs) that are a combination of one GOODS like field (with 120 objects on average) plus an UDF-like field (with 100 objects on average) for the three different fitting methods considered in the paper. [*See the electronic edition of the Journal for a color version of this figure.*]

of the halos above a minimum mass threshold within the selection window for Lyman break galaxies at different redshifts (corresponding to *V*, *i*, *z*, and *J* dropouts for *HST* surveys). In addition, we also consider *JWST* NIRCam F115W, F150W, and F200W dropouts up to $z = 15$.

By populating the dark matter halos with galaxies using different semianalytical prescriptions, which include multiple halo

occupation and different detection probabilities, we have shown that, to first order, the standard deviation of the number counts for a given dropout population depends mainly on the average value of number counts and on the geometry of the pencil beam. This is because the average bias of the population varies little as a function of the number density and is reassuring for the robustness of our results, as it means that the still uncertain details of high-redshift

galaxy formation are unlikely to significantly affect the amount of cosmic variance in deep surveys.

The distribution of the number count around its central value is highly skewed for low number counts, while it becomes progressively more symmetric as the average number of objects in the field of view increases. The ratio of the measured variance to the variance expected from Poisson noise is an increasing function of the average number of objects in the field. For the typical number counts of V and i-dropout in an ACS field of view at the UDF depth, the $1\,\sigma$ fractional uncertainty is about 3 times that due to Poisson noise. This has a major impact on the rarity of overdensities of high-redshift galaxies such as those reported by Malhotra et al. (2005), which, while highly significant with respect to a Poisson statistics, turn out to be not uncommon when the effect of clustering is taken into account (e.g., at the $1.5\,\sigma$ level in the Malhotra et al. 2005 case).

The geometry of the volume probed is fundamental in defining the number count variance, and a long and narrow beam has a lower variance than that estimated from an equivalent spherical (or cubical) volume. This is because the long beam passes through many different environments, while a spherical volume may happen to sit right on top of extreme overdensities or underdensities. For example, for i-dropouts an ACS like field of view of $6 \times 6 \times 320$ (Mpc $h^{-1})^3$ has a fractional uncertainty of $\approx 30\%$ for 100 counts on average, while an equivalent cubic volume would have an uncertainty of $\approx 50\%$.

Number counts in nearby fields are significantly correlated: for i-dropouts, two adjacent ACS fields with 50 i-dropouts counts on average have a linear correlation coefficient $r_{\rm lin} = 0.41$. This becomes $r_{\rm lin} \lesssim 0.05$ at angular separation of about $550''$. This has two important consequences: (1) large-area surveys with adjacent exposures such as GOODS are still affected by a non-negligible amount of cosmic variance, so that v_r is of the order of $\approx 20\%$ for i-dropouts down to its faint detection limit and combining the two North and South fields, and (2) *HST* parallel observations, separated by about $600''$, such as those from the UDF and UDF follow-up programs, can be considered essentially independent fields. For independent fields, the cosmic variance decreases as the square root of the number of fields (in fact, the variance from independent variables sums up in quadrature). From the point of view of future observations, this also implies that the currently existing six ultradeep NICMOS fields have a smaller total cosmic variance than a future single WFC3 deep field to comparable depth, despite the greater area of the latter.

Using a simple mass-luminosity relation (eq. [6]), we also investigate the effects of cosmic variance on the determination of the galaxy luminosity function. The impact of cosmic variance is not limited to the normalization of the luminosity function, but extends also to its shape. In fact, the luminosity function for underdense regions appears to be steeper than for field and cluster environments. By fitting a Schechter function to synthetic

catalogs of V-dropout galaxies in a UDF-like survey, we find that M_* varies by about 1 mag from overdense to underdense fields, while the slope α remains approximately unchanged. An important caveat is that, as we have taken into account essentially only dark matter clustering in our modeling, our result could change if strong feedback effects due to baryon physics are important.

This dependence of the luminosity function on the number counts of the field has important consequences when attempts are made to correct for a deficit of detections in data sets that combine a large area survey with a small, deeper area. In fact, an artificial steepening of the estimated luminosity function from binned data may arise when naive corrections to account for underdensities are used, such as a renormalization of the faint end of the luminosity function in terms of the ratio of bright counts in the deep area of the survey with respect to the average value of bright counts over the whole survey area.

Therefore, to determine the luminosity function for such survey configurations, the best approach appears to be the maximum likelihood method applied to the unbinned data, as originally proposed by Sandage et al. (1979). The first step is to determine the shape (α and M_*) of the Schechter function probability distribution, convolved with a detection probability kernel to take into account incompleteness and selection effects. This can be done by combining the likelihood of both faint and bright counts, but allowing the normalization ϕ_* to be a free parameter and to vary among the two samples. Next, ϕ_* is estimated from the total number counts of the two samples, compared with the expectation from integrating the luminosity function between the relevant luminosity limits. This method appears to be relatively unbiased with respect to cosmic variance, and represents an approach that does not require quantifying the relative normalization of the detections in the different fields considered.

Finally, we stress that the intrinsic uncertainty due to cosmic variance present while estimating the luminosity function parameters must be taken into account when claims are made regarding the redshift evolution of these parameters. For example, by combining one GOODS-like field with a single deep, UDF like field, cosmic variance introduces a $1\,\sigma$ uncertainty in α of $\Delta\alpha \approx 0.15$. This error is a systematic contribution that comes on top of any other contribution to the total error budget.

REFERENCES

Beckwith, S. V. W., et al. 2006, AJ, 132, 1729
Bertschinger, E. 2001, ApJS, 137, 1
Bouwens, R. J., et al. 2004, ApJ, 606, 25
Bouwens, R. J., Illingworth, G. D., Blakeslee, J. P., & Franx, M. 2006, ApJ, 653, 53
Bouwens, R. J., Illingworth, G. D., Franx, M., & Ford, H. 2007, ApJ, 670, 928
Bunker, A., Stanway, E., Ellis, R., McMahon, R., Eyles, L., & Lacy, M. 2006, NewA Rev., 50, 94
Colombi, S., Szapudi, I., Jenkins, A., & Colberg, J. 2000, MNRAS, 313, 711
Cooray, A. 2005, MNRAS, 364, 303
Cooray, A., & Milosavljević, M. 2005, ApJ, 627, L89
Eisenstein, D. J., & Hu, W. 1999, ApJ, 511, 5

Eisenstein, D. J., & Hut, P. 1998, ApJ, 498, 137
Gardner, J. P., et al. 2006, Space Sci. Rev., 123, 485
Giavalisco, M. 2002, ARA&A, 40, 579
Giavalisco, M., et al. 2004, ApJ, 600, L93
Hoyle, F., Rojas, R. R., Vogeley, M. S., Brinkmann, J. 2005, ApJ, 620, 618
Kitzbichler, M. G., & White, S. D. M. 2007, MNRAS, 376, 2
Madau, P., Ferguson, H. C., Dickinson, M. E., Giavalisco, M., Steidel, C. C., & Fruchter, A. 1996, MNRAS, 283, 1388
Malhotra, S., et al. 2005, ApJ, 626, 666
Mo, H. J., & White, S. D. M. 1996, MNRAS, 282, 347
Mobasher, B., et al. 2005, ApJ, 635, 832
Newman, J. A., & Davis, M. 2002, ApJ, 564, 567
Oesch, P., et al. 2007, ApJ, 671, 1212

Ouchi, M., et al. 2005, ApJ, 620, L1
Overzier, R. A., Bouwens, R. J., Illingworth, G. D., & Franx, M. 2006, ApJ, 648, L5
Peacock, J. A., & Dodds, S. J. 1996, MNRAS, 280, L19
Peebles, P. J. E. 1993, Principles of Physical Cosmology (Princeton: Princeton Univ. Press)
Press, W. H., & Schechter, P. 1974, ApJ, 187, 425
Sandage, A., Tammann, G. A., & Yahil, A. 1979, ApJ, 232, 352
Scoville, N., et al. 2007, ApJS, 172, 1
Sheth, R. K., & Tormen, G. 1999, MNRAS, 308, 119
Somerville, R. S., Lee, K., Ferguson, H. C., Gardner, J. P., Moustakas, L. A., & Giavalisco, M. 2004, ApJ, 600, L171
Spergel, D. N., et al. 2007, ApJS, 170, 377

Springel, V. 2005, MNRAS, 364, 1105
Steidel, C. C., Giavalisco, M., Pettini, M., Dickinson, M., & Adelberger, K. L. 1996, ApJ, 462, L17
Stiavelli, M., Fall, S. M., & Panagia, N. 2004, ApJ, 610, L1
Szapudi, I., Colombi, S., Jenkins, A., & Colberg, J. 2000, MNRAS, 313, 725
Trenti, M., & Stiavelli, M. 2006, ApJ, 651, 704
Vale, A., & Ostriker, J. P. 2004, MNRAS, 353, 189
Verma, A., Lehnert, M. D., Förster Schreiber, N. M., Bremer, M. N., & Douglas, L. 2007, MNRAS, 377, 1024
Wechsler, R. H., Somerville, R. S., Bullock, J. S., Kolatt, T. S., Primack, J. R., Blumenthal, G. R., & Dekel, A. 2001, ApJ, 554, 85
Williams, R. E., et al. 1996, AJ, 112, 1335
Yan, H., & Windhorst, R. A. 2004, ApJ, 612, L93